Mechanical and functional properties of Invar alloy for μ-MIM

J. Hidalgo, A Jimenez-Morales, Thierry Barriere, Jean Gelin, José Manuel Torralba

Mechanical and functional properties of an invar alloy for µ-MIM

J. Hidalgo[1], A. Jiménez-Morales[1], T. Barriere[2], J.C. Gelin[2], J.M. Torralba[1,3]

1 Carlos III University of Madrid, Avd. Universidad 30, 28911 Leganés (Spain) jhidalgo@ing.uc3m.es, toni@ing.uc3m.es.
2 University of Franche-Comté, 26 rue l'Epitaphe, 25000 Besançon (France), thierry.barriere@univ-fcomte.fr
3 Institute IMDEA Materials, Eric Kandel 2, 28906 Getafe (Spain), josemanuel.torralba@imdea.org

Abstract

Micro metal injection moulding (µMIM) is a promising alternative for fabricating micro parts. Low coefficient of thermal expansion (CTE) Fe_x-Ni_{1-x} alloys are suitable to meet high dimensional stability with temperature keeping acceptable mechanical properties. However these alloys are sensible of elements contamination during the debinding and sintering stages and their dimensional stability and mechanical properties could be affected. The present work studies the effect of using combinations of debinding and sintering atmospheres in the µPIM of Invar 36 feedstocks based on cellulose acetate butyrate (CAB) binders. Micro-tensile specimens were successfully injected. Densification and microstructure at different conditions were linked with mechanical and physical properties of the parts. The processing conditions and thus the residual C, O and especially H influence severely these properties.

Keywords: Invar 36, cellulose acetate butyrate, polyethylene glycol, micro-MIM, sintering atmospheres.

1. Introduction

Powder metallurgy (PM) of Fe_x-Ni_{1-x} of low coefficient of thermal expansion (LCTE) alloys presents several processing advantages with respect casting. Energy and cost savings and a reduction of elements segregation risk could be achieved, thus increasing alloy properties [1]. Furthermore, PM can reduce tedious and time consuming machining steps that are specially complicated for Fe_x-Ni_{1-x} LCTE alloys due to their high ductility and low thermal conductivity. It is also greatly complicated to maintain Invar properties when joining by fusion welding. Such welding results in solidification cracking, porosity and reheating cracking when a matching CTE filler metal is used [2]. Metal injection moulding (MIM) design versatility may also eliminate the needs of joints by welding. To that respect MIM emerges as a cost-effective solution for near net-shape fabrication of complex geometry small pieces [3]. Examples of potential MIM application of LCTE alloys are wide in the field of high precision devices like in optoelectronic or light wave communication systems, housing or structural components [4]. Currently, there is an increasing demand of miniaturised components for micro devices like micro gears or micro actuators [5-8] in which micro metal injection moulding (µ-MIM) of low CTE alloys could be an interesting alternative.

The abnormal LCTE behaviour within metals, which normally considerably expand with heat and contract with cold, is consequence of the so-called Invar (volume INVARiance) effect. The physical mechanism explaining Invar effect still remains uncertain, but from general standpoint low expansion occurs due to two opposing effects over a specific temperature range. During heating, the alloy naturally expands while simultaneously a ferromagnetic-to-paramagnetic transformation imposes a magnetostriction that counteracts the expansion [9, 10]. The minimum CTE in the binary iron-nickel alloying system occurs in the composition $Fe_{0.65}$-$Ni_{0.35}$, the commercial Invar 36, which also has one of the lowest CTE of any alloy from room temperature to about 230ºC (the 4.5% cobalt modification has almost zero expansion over that range). Microstructure of Fe_x-Ni_{1-x} LCTE alloys commonly consists of a substitutional solid solution of nickel in iron creating an austenitic face centred cubic lattice. The austenitic γ phase, that is present at all temperatures, shows a high ferromagnetism at temperatures below the Currie temperature, and a paramagnetic behaviour above this temperature. Heterogeneities in the cast alloy and the presence of other elements like carbon introduce the possibility of formation of Ni segregation regions within the γ lattice [11-14]. Therefore low moment (LM) paramagnetic Fe-rich phases could coexist with clusters of Ni-rich high moment (HM) ferromagnetic order phase negatively affecting CTE. Furthermore a martensitic phase could be formed for quenched alloys which also degrade low expansion properties. However, elements like C and Ni act as a γ phase stabilizers diminishing the martensitic temperature (Ms). Concentrations below about 33 at.% Ni lead on structural transitions from γ to a body centred cubic phase α which does not show the Invar effect. Carbon presence could stabilize γ phase for concentrations below 33 at.% Ni.

Table 1 Mechanical properties of different Invar 36 materials.

Material	YS [MPa]	UTS [Mpa]	Strain to breakage [%]	H_v [Gpa]
Wrought Invar 36 (ASTM A658)	> 241	448-552	> 30	N/A
Wrought Invar 36[15]	275	490	40	1.30
High purity PM Invar 36 extruded[16]	271	468	70	N/A
Invar 36 (0.06 C)	310	N/A	N/A	1.5-1.6
Invar 36 ECAP 2 passes[17]	570	732	47	2.42
Invar 36 ECAP 12 passes[17]	835	912	52	2.60

Dimensional stability has to be accompanied with good mechanical properties. Table 1 shows some typical mechanical properties of Invar 36 alloys processed under different conditions. Invar 36 ordinary wrought alloy [15] and high purity powder-metallurgy-route processed alloy [18] have relatively low strength, but high ductility. Age hardening by some by addition of elements (Ti, Al, Sn, etc) is an alternative to enhance Invar 36 properties. Nonetheless the CTE, which is the property of primary importance in these alloys, increases with both aging and concentration of additions [19]. Small amounts of carbon could be beneficial to improve mechanical properties

while an acceptable low CTE is maintained [14, 20]. Carbon presumably affects mechanical properties by strengthening the interstitial solid solution. Moreover, creating ultra-fine grain structures by e.g. severe plastic deformation using equal-channel angular pressing (ECAP) has demonstrate to significantly increase mechanical properties without scarifying low CTE[17].

The present work studies the effect of debinding and sintering atmospheres in the mechanical and physical properties of Invar 36 micro parts. A binder composed of cellulose acetate butyrate (CAB) and water soluble polyethylene glycol (PEG) was used in the μMIM process. CAB thermoplastic polymers have been successfully employed for PIM proposes in several references [21, 22]. Nevertheless CAB does not degrade completely during thermal elimination step if a protective atmosphere is employed during debinding [23]. The residual carbon could be introduced in alloying system in further steps altering alloy properties. Air atmosphere is able to completely degrade CAB due to organic compounds oxidative reactions with oxygen but also oxidises metallic powders at typical debinding temperatures. Residual carbon introduced by CAB during debinding might be eliminated in presence of hydrogen, oxides or vacuum during sintering. However there is the concern of possible carbon contamination that would affect the part properties as well as interstitial hydrogen if this atmosphere is used. Taking into account all these facts, different debinding and sintering atmospheres have been used to study their effect in the sinterability, microstructure and elements contamination of Invar 36 micro parts. These results were linked with mechanical and physical properties. Micro tensile and hardness test were conducted and the coefficient of thermal expansion and Curie's temperature evaluated depending on the processing conditions.

2 Experimental processes

Gas atomized spherical INVAR 36 alloy powders were used in this study. The INVAR 36 alloy consists of 36 wt% of Ni and Fe balanced except some other elements traces. The composition of the INVAR 36 alloy is shown in Table 2 along with the particle size parameters. The powders were supplied by Sandvik Osprey Ltd. (UK). The powder has a particle size distribution with a D90 of 5.9 μm. The small size of the powders will allow a good reproducibility of the shape with smooth surfaces and a minimum part section of about 60 μm.

Table 2 Composition and particle size distribution parameters for Invar 36 powders

Composition	**Ni**	**Mn**	**Si**	**C**	**O**	**Fe**	**Particle Size Distribution**	**d_{10}**	**d_{50}**	**d_{90}**
[mass%]	36.50	0.20	0.02	0.01	0.13	Balanced	[μm]	1.9	3.4	5.9

Each powder was mixed with a binder system based on a combination of several thermoplastic polymers, employing poly (ethylene glycol) (PEG) (supplied by Sigma-Aldrich) of different molecular weights and two

types of cellulose acetate butyrates (CAB) (supplied by Estman) with a variable content of acetyl, butyryl and hydroxyl groups. The binder component content and component specifications are included in Table 3.

Table 3 Binder composition

Component	Acetyl*	Butyryl*	Hydroxyl*	%vol
CAB381-0.1	13	37	1,5	30
CAB551-0.01	2	53	1,5	10
PEG 20k	-	-	-	58
PEG 4k	-	-	-	2

** Percentage of side groups in chain*

A feedstock with a powder solid loading fraction of 65 vol.% was prepared in a Haake Rheomex twin sigma rotor internal mixer. The feedstock was mixed at a temperature of 150ºC and a rotor speed of 50 rpm for one hour to ensure the homogenisation of all components. The feedstock was employed to perform a full µPIM process. Injection of tensile and bending test micro parts was carried out by a Battenfeld Microsystem 50 microinjection moulding machine. Green micro parts were subjected to a two steps debinding process. First a solvent debinding in water media at 30 ºC was carried out previous to a thermal debinding. Then, two types of atmospheres were used during thermal debinding, air or vacuum, trying to achieve different levels of residual carbon and oxides. During thermal debinding, specimens were heated up to 400 ºC with a heating rate of 2 ºC/min and this temperature was held during 30 minutes.

Brown parts were sintered at 1100 ºC and with a heating rate of 5 ºC/min in vacuum or hydrogen atmospheres. Sintering temperatures were held during 60 minutes. Therefore four types of sintered parts were obtained: debinding in vacuum – sintering in vacuum (V-V), debinding in vacuum – sintering in hydrogen (V-H), debinding in air – sintering in vacuum (A-V) and debinding in air – sintering in hydrogen (A-H). Examples of different green, brown and sintered parts are shown in Figure 1. The narrowest section of the parts corresponds to the tensile test sample with 0.7mm x 0.7 mm. However the runners of both parts have a diameter of 0.3 mm.

Sintered parts were characterised in terms of microstructure investigation with a Philips XL-30 scanning electron microscope (SEM) and a Philips X'Pert X-ray diffractometer. Sinterablity was assessed by three methodologies: relative density measurement by Archimedes immersion method, determination of porosity by image analysis and shrinkage by comparing green and sintered part dimensions. For the image analysis, light optical microscope (LOM) images of ten different regions within the polished part cross section were evaluated and an averaged value with the standard deviation presented. The specimens preparation, the brightness and contrast parameters used to discriminates features, the number of fields examined, the total surface examined and the magnification

of the objective lenses were optimised to obtain the most reliable and comparable results possible. In this case the magnification was settled at x2000.

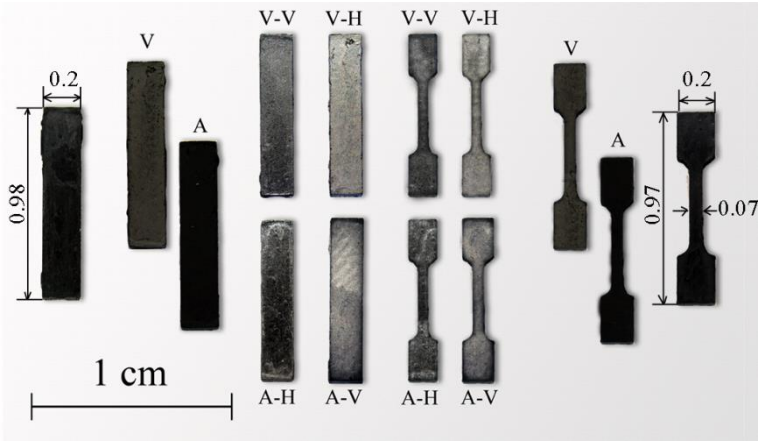

Figure 1 Green, Brown and sintered parts after different processing conditions: A: air, V:vacuum, H:hydrogen.

Residual carbon and oxygen content was measured by ThermoFischer Scientific Flash 2000 CHNS/O elementary analyser. Curie temperature that determines the end of the almost constant low thermal expansion temperature range in invar alloys was evaluated with a TA Instruments Q50 thermogravimeter coupled with a magnet placed always at the same distance to the sample. The ferromagnetic to paramagnetic transition is determined with a suddenly drop in the registered sample weight. The linear coefficient of thermal expansion was evaluated from room to 350 ºC at 5 ºC/min in a TA Instruments TMA. It uses a simple rod, hence the data presented are not absolute CTE but they still provide valuable information when the CTE's of the processes were compared. A Kammrath and Weiss micro-mechanical testing stage with a load cell of 1 kN was used to perform micro tensile tests at room temperature. This was coupled with a Zeiss EVOMA 15 SEM to perform in situ micro mechanical tests. A fractography analysis was carried out after the tests. Finally, the specimens' microhardness was obtained by a Time Technology Europe digital microhardness tester HVS-1000.

3 Results

3.1 Densification and elements analysis after sintering

After sintering in different atmospheres and at different heating rates the sinterability of the resulting parts was evaluated by different methodologies. Figure 2 shows the highly illuminated and contrasted LOM images of the cross section of the parts. In Figure 3, the relative density by Archimedes immersion method, the densification assessed by the ratio between the pore area to total area and the shrinkage values are presented. There were differences between the relative densification measured by Archimedes method and image analysis. This could be attributable to the presence of macro porosity in some areas of the parts or to the parameters chosen by image

analysis. Nevertheless, the tendency was the same in both cases. The residual carbon and oxygen content were also determined and the results were collected in Table 4.

Table 4 Carbon and oxygen contents for different processing conditions

	Powder	Debinding		Sintering			
		A	**V**	**A-V**	**A-H**	**V-V**	**V-H**
C [mass%]	0.01	0.12	0.73	0.06	0.06	0.06	0.05
O [mass%]	0.12	0.57	0.15	0.38	0.07	0.13	0.10

Labrador [24] studied the oxidation kinetics of a wrought Invar 36 alloy in air. The oxidation in terms of mass gains begins to be appreciable above 580 ºC, with the exclusive formation of porous iron oxides specially Fe_2O_3 but also Fe_3O_4 and FeO. Metallic oxide layers in the powder surface inhibit the atom diffusions and thus the sintering mechanism being this fact detrimental for densification of the sintered parts. Reductive conditions (hydrogen, vacuum or CO atmospheres) during sintering could act in the oxide layer enhancing sintering mechanisms. The thermodynamic data calculated using thermodynamic modelling software (HSC Chemistry 7.1) reveal that at 1100 ºC oxygen partial pressures of approximately 10^{-13} bar are needed to decompose the different iron oxides. Below this temperature, partial pressures have to be lowered to achieve the same effect. Carbon may also participate in the oxide reduction essentially in two stages [25, 26]. The first involves the reduction of surface oxides which are in contact with residual binder organic compounds during the heating stage. This reaction is the so called direct carbothermal reduction. The produced carbon monoxide can further react with the existing oxides towards the formation of carbon dioxide. This reaction in turn is called indirect carbothermal reduction. Direct and indirect carbothermal reductive reactions become more important above 720 ºC since then the equilibrium in the Boudouard reaction is shifted towards the formation of carbon monoxide which is the more stable product from this temperature and above. Regarding hydrogen as a reductive atmosphere, the reductive effect will depend on the water vapour partial pressure, the heating rates, the velocity and concentration of hydrogen. Jozwiak et al. [27] evaluates these parameters influence on the reduction of different iron oxides by hydrogen and concluded that the complete reduction of these oxides into metallic iron phase can be accomplished at a relatively low temperature, below 380 ºC. However this temperature shifted to higher temperatures as the heating rates are increases (around 750 ºC at 10 ºC/min). More over the effectiveness of the reduction was is strongly influenced by their size and crystallinity and presence of other metals.

The A-V turned out to be the most unfavourable condition in terms of densification and shrinkage due to the presence of oxide layers surrounding powder particles formed most likely during debinding. This was coherent with the high oxygen content measured in this condition in both brown and sintered parts compared to the

original oxygen content of the powder. Although the vacuum condition may cause a reductive effect, the oxides layers were probably stable at sintering conditions and hindered the diffusion of the metallic atoms. However it is worth to note that there was a considerable reduction of the oxygen content comparing the brown and sintered parts. This would be explained by a direct or indirect carbo-reductive effect of the remaining carbon after debinding aided by the low pressures.

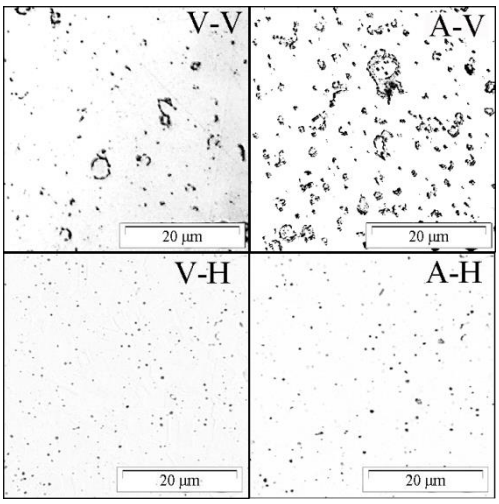

Figure 2. Highly contrasted LOM images of different grinded and polished Invar 36 micro parts at the same magnification for the evaluation of the densification and the remaining porosity. The specimens were not etched in this case.

In the V-V condition parts, some original powder particles were still observed as it occurred in A-V parts. The number of these original powder particles was considerably lower than in the A-V conditions as well as the proportion and size of pores observed. The oxygen measured in the V-V parts was lower than the A-V part but comparable to the corresponding brown part measured after debinding. These brown parts has slightly higher oxygen content than the original particles, thus it can be concluded that vacuum debinding atmosphere was effective to preserve particles from oxidation.

The parts sintered in hydrogen, independently of the debinding atmosphere, demonstrated to have a higher volumetric shrinkage factor and thus a better densification. They showed a homogeneous porosity distribution and the absence of original powder particles. These results were consistent with the low oxygen contents of these parts which demonstrated an efficiently reduction of the oxides by the hydrogen.

The measured carbon content was comparable in all conditions and was higher than the original powder particles. This denoted that there is a carbon contamination that cannot be avoided by any of the selected processing conditions. The carbon contents were still low but this contamination might affect the Invar properties.

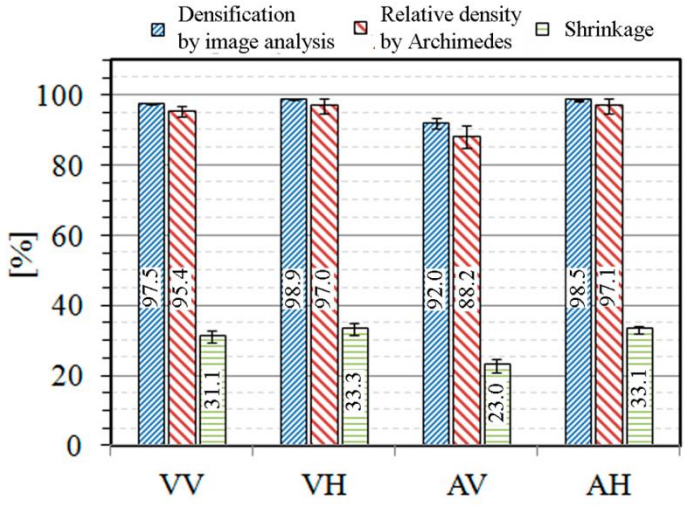

Figure 3.Sinterability study of the micro parts by different methodologies. The percentage of porosity was assessed by image analysis software. The relative density was measured comparing Archimedes method density with respect to the Invar 36 powders density. The shrinkage of the part was evaluated by direct measurement of the sintered part dimensions and comparing them with green part dimensions.

3.2 Microstructure analysis and phases determination by XRD

Figure 4 shows back scattering electron detector SEM images of INVAR 36 micro-parts cross sections representing different debinding and sintering conditions. With the exception of A-V parts (Figure 4 b) the rest of conditions developed a clear austenitic microstructure with typical austenite twin bands. The presence of a γ' Ni rich phase is not discarded but was not detected by SEM inspections. Sometimes γ' precipitates are in the order of nm which is out of the SEM range. In the same way graphite precipitates were not detected. The grain size of the austenite varied depending on the processing condition with apparently the bigger grains detected for the V-H condition (Figure 4 c). The big austenite grains of V-H made thinking on a prompter initiation of the elements diffusion mechanisms compared with other conditions. This would be explained by a rapid reduction of the particle surface oxide at earlier stages of the sintering. Comparing V-V and A-H conditions, the last seemed to have lower grain sizes. Finally, A-V condition had the smallest grain sizes in the order of powder particle size.

The pore sizes seemed to be higher than those observed in LOM by image analysis, but the proportion of porosity was similar and more coherent with the Archimedes measurements. However, in these cases the samples were etched and the porosity may be broadened. It is worth to note the roundness and the small sizes of the pores which were related to the ending stages of the sintering. The effectiveness of the sintering at 1100 ºC may be explained by the small powder particle size that is well established to promote sintering; as powders become finer, sintering activity increases and full density can be achieved at lower temperatures. Imbaby et al. [28] reported that 99% density is obtained from 90%-4µm 316L powder at 1200 ºC.

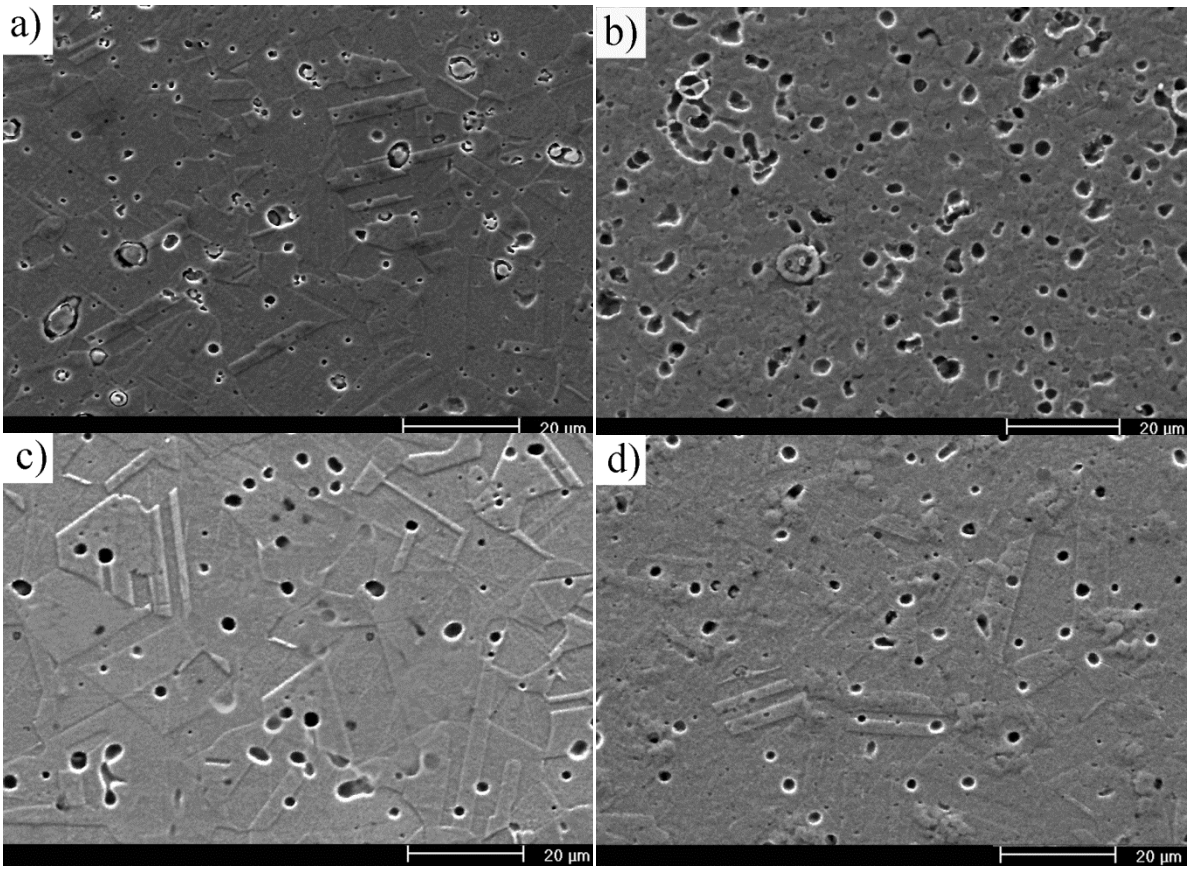

Figure 4 Secondary scattered electron detector SEM images of cross sections of different processing conditions INVAR 36 micro-parts: a) Vacuum-vacuum, b) air-vacuum, c) vacuum-hydrogen, d) air-hydrogen. The parts were etched with *aqua regia* a solution of concentrate nitric acid and concentrate hydrochloric acid in a volume ratio of 1:3.

As it was already observed by LOM, in case of sintering in vacuum conditions, some original powder particles that apparently had not take part of the sintering mass transfer mechanism were observed. However, some differences could be appreciated when comparing V-V or A-V. The main difference was the thickness of the oxide layer around particles. A thick dense oxide layer without fissures surrounded powder particles in case of A-V parts (Figure 5a) whereas a thin oxide layer with some discontinuities embedded powder particles in case of V-V parts (Figure 5b); in these discontinuities sintering necks had began to be formed. The residual carbon in V-V combined with a vacuum atmosphere had a reductive effect but it was not enough to reduce all the oxides. In the A-V and V-V SEM images the number of original particles was similar. This seems to contradict Figure 2 results were more original particles were observed in A-V condition. This may be explained by a combined effect of an etching media with ultrasound bath surface cleaning that made some particles to be removed from the surface of A-V condition. The fracture surfaces in Figure 11 again showed a higher density of original particles in the case of A-V condition.

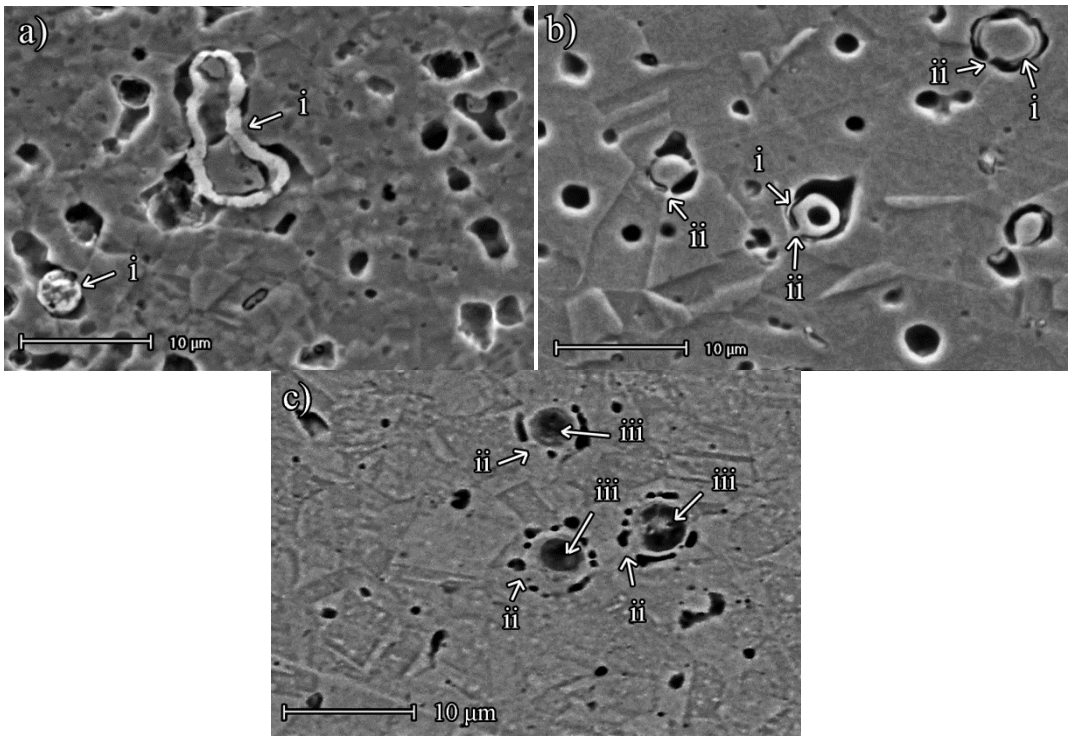

Figure 5 Secondary electrons detector SEM micrographs of cross sections of INVAR 36 sintered micro-part: a) A-V, b) V-V c) A-H. (i. oxide layer, ii. sintering neck, iii. micro void formed due to elements diffusion)

The absence of oxides in hydrogen sintered parts evidenced the efficacy of the reductive effect of a hydrogen atmosphere. However, some original particles were sporadically observed in A-H conditions (see Figure 5c). They were in a very advanced sintering stage with the entire surrounding oxide layer reduced and with lot of sintering necks. This was not observed in V-H parts. The oxide layer generated during debinding in air most likely was thicker than debinding in vacuum as it could deduced from A-V micrographs. Hence the A-H parts would need more time to end with the oxide layer reduction than V-H parts, and thus some particles are still at the end stages of the sintering. This also would explain the differences in grain sizes.

During SEM inspections SiO_2 and other complex oxides inclusions were found. Silica particles are often observed sintered materials because a small amount of silicon, <0.8%, is usually added into the melt to facilitate atomization. Silica particles are difficult to reduce, even though using hydrogen atmospheres, especially at 1100 ºC.

When XRD analyses were conducted to determine the phases formed during the different consolidating processes, similarities were observed in the resulting diffractograms. In all cases, as could be observed in Figure 6, austenitic γ(FCC) phase characteristic of $Fe_{0.64}$-$Ni_{0.36}$ was clearly identified and almost perfectly indexed by comparing peaks positions with XDR patterns. Nevertheless there were divergences in the relative peaks intensities patterns and occurrence of double peaks. The double peaks at high angles was associated to Cu-$K_{\alpha 2}$

radiation as the second peak is displaced to higher angles and had almost the half of the intensity of the most intensive first peak. However at lower angles these double peaks of similar intensities could be associated with heterogeneities in the composition due to Ni segregations and lattice distortions caused by interstitial elements. For the original powders and for the A-V condition, small intensity peaks associated with a α BCC phase were detected. This fact was predictable since the non reduced oxide layer likely would have impeded the elements homogenisation by diffusion mechanisms, in case of having heterogeneous particle compositions and α particles.

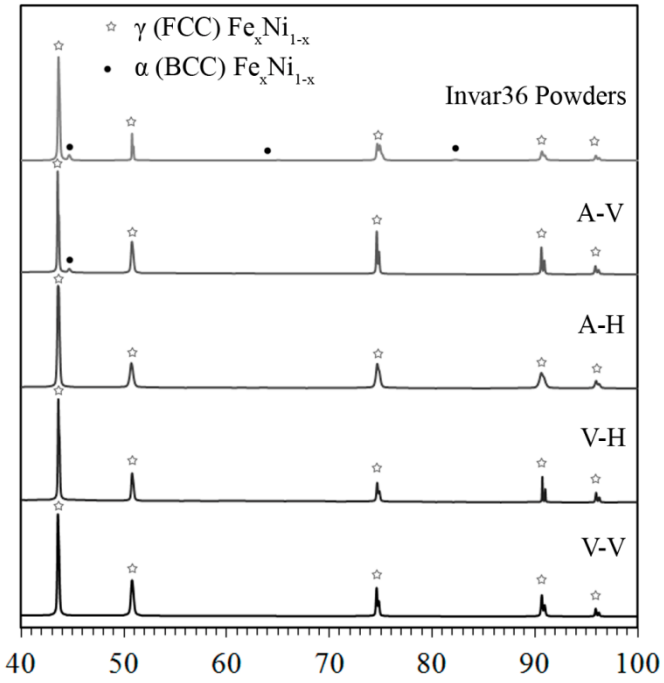

Figure 6 XRD diffractograms and phases identification of sintered parts subjected to different debinding and sintering conditions: a) vacuum-vacuum, b) air-hydrogen, c) vacuum-hydrogen, d) air-vacuum.

3.3 Coefficient of thermal expansion and Curie temperatures

Figure 7 shows a TGA weight loss (dashed line) associated with the Invar 36 ferromagnetic to paramagnetic transition, i.e. the Curie temperature. During this transition, a magnet positioned close to the sample stopped attracting it when the paramagnetic state occurred. The derivative of the curve represents the characteristic Curie temperature peak defined by its maximum, the offset and the width. Table 5 collects the results of the different processing conditions micro parts and of the original powders. Comparing the values, there was a reduction of the Curie temperatures in the sintered parts compared with the original powders. This could be associated with the presence of interstitial elements (C or H) or Ni segregations. This variation was more severe in the sintered in hydrogen parts which remarked the negative effect of the hydrogen in this property. The wide peak registered for the powder particles may be associated with heterogeneities in the composition of different powders and/or the particle size distribution. The Curie's temperature has demonstrated to be influenced by composition and by the

austenite grain size. This would also explain the double peak detected in the A-V condition which apparently showed the lowest grain size and also original powder particles.

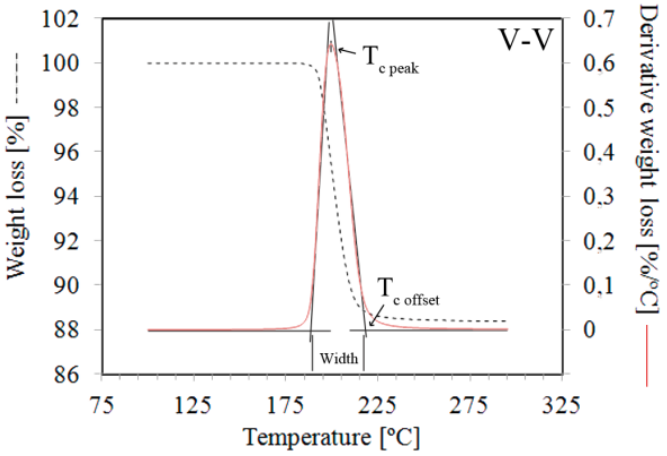

Figure 7 TGA weight loss (dashed line) associated with the Invar 36 ferromagnetic to paramagnetic transition. The derivative of the curve represents the characteristic Curie's temperature peak defined by its maximum, the offset and the width.

Table 5 Curie temperatures for different parts processed with different atmospheres

Tc [ºC]	INVAR Powder	V-V	V-H	A-V		A-H
Peak	221.2	199.4	185.7	213.7	236.7	186.7
Offset	282.2	216.0	196.4	245.4		201.6
Width	89.1	27.3	20.4	42.4		25.8

Figure 8 plots the linear coefficient of thermal expansion (CTE) at different temperatures of different debinding and sintering conditions. The small dimensions of the samples caused noise in the measurements of the expansion with temperature curves, thus smoothing had to be carried out to determine the linear CTE by the following expression:

$$CTE_{linear} = \frac{1}{L_0} \cdot \frac{\Delta L}{\Delta T} \qquad (1)$$

where L_0 is the initial length of the sample and ΔL represents the variation of length at a certain increment of temperature ΔT. Smoothing and the use of a simple rod dilatometer may produce some errors in the assessment of the linear CTE. Therefore the data presented are not absolute CTE but they still provide valuable information when the CTE's of the four processes were compared. The values obtained and the behaviour with temperature and processing conditions seemed to be consistent with the Curies' temperature results and with the intrinsic behaviour of an Invar 36 alloy. At temperatures below the T_c, the CTE was low (in the order of 1.3 $10^{-6}\cdot ºC^{-1}$to 3 $10^{-6}\cdot ºC^{-1}$) and relatively steady. Near the T_c this tendency changed and the CTE values began to raise with temperature up to values were the curve seemed to stabilise again at temperatures above the T_c. The CTE at high temperatures was in the order of those for stainless steels. As it occurred with the T_c there was a

clear effect of the sintering in hydrogen conditions in the CTE values. These conditions showed the worst values of CTE at all the temperature range.

A-V condition resulted to give the best CTE results. The reason explaining this fact was unclear, especially considering that some alpha phase was developed in these parts (as reflected in XRD analysis). A combined effect of Invar 36 low CTE until around 200 ºC and the low CTE of non-reduced oxides at higher temperature may be a plausible explanation. Moreover, the small grain size may be also influencing the results.

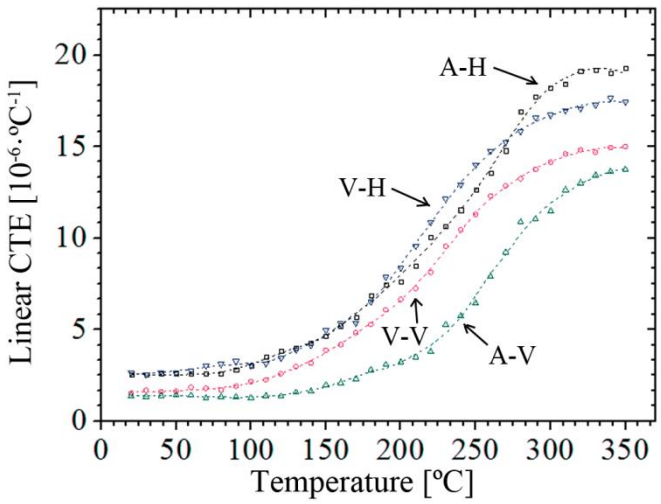

Figure 8 Linear coefficient of thermal expansion at different temperatures of different debinding and sintering conditions.

3.4 In situ tensile and hardness micro mechanical test

Figure 9 shows the representative strain-stress curves of different processing conditions. Table 6 collects some characteristic mechanical parameters according to these curves. Zhao et al. [29] discussed the limitations and issues in correctly interpreting micro tensile experiments. The micro test experimental studies assume errors in the strain measurements as the data were collected directly from the cross head displacement without any extensometers, digital image correlation or laser interferometry. Thus, only engineering results are presented in this work. However, as the tests were performed on the same device, the results are considered valid for comparative purposes.

The ASTM Designation A658 covers 36 percent nickel-iron alloy and specifies a tensile strength of 448-552 MPa, a minimum yield strength (0.2% offset) of 241 MPa and a minimum elongation of 30%. Although these values are representative of the wrought Invar 36, the results derived from the micro-tests of powder consolidated specimens were consistent with these specifications and the values collected in Table 1. However

there was a great diminution of the strain and thus of the ductility in the sintered in hydrogen parts. This coincided with the highest yield strength values registered.

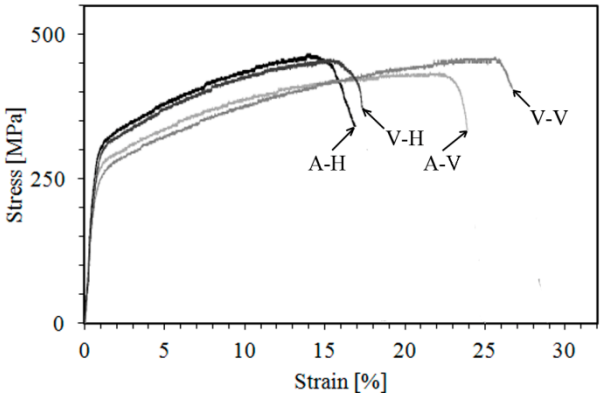

Figure 9 Representative stress-strain curves of different processing conditions.

Considering that the porosity values in V-V, V-H and A-H conditions were similar as well as the carbon content, it could be stated that hydrogen was the responsible of this embrittlement effect. However, the ultimate tensile stress (UTS) values were similar for those conditions. The lowest UTS was registered by the A-V condition and it is probably associated with the high porosity of these parts. The presence of oxides also limits the elongation values in comparison with the V-V condition. These results were consistent with the microhardness results. The highest HV corresponded to the sintered in hydrogen part evidencing the low ductility results. The lowest value corresponded to the A-V condition, most likely due to the high porosity. The micro hardness values were also in the range of the Invar 36 materials (see Table 1).

Table 6 Micro-mechanical properties of different processing conditions

	A-H	A-V	V-H	V-V
UTS [MPa]	466±15	436±22	458±15	462±19
Strain to fracture [%]	17±1	22±2	18±1	28±2
Yield strength (0.2% offset) [MPa]	290±12	252±21	267±15	212±19
H_V/9.8N [GPa]	1.70±0.021	1.2±0.023	1.69±0.020	1.63±0.021

A representative behaviour of the microstructure evolution with the applied stress in Invar 36 micro parts is shown in Figure 10, corresponding to V-V condition. No significant differences were observed for the rest of the conditions. At stresses near the yield point, a small deformation of the austenitic grain was observed but no other differences were observed in the microstructure comparing the images with the uncharged condition. Above the yield point the austenitic grain deformation became appreciable as well as the formation of slip bands. The deformation and the density of the slip bands were considerable near the UTS. The round pores were elongated in the strain direction and some of them begin to coalesce. At fracture, slip bands moving from different sliding directions were observed crossing over.

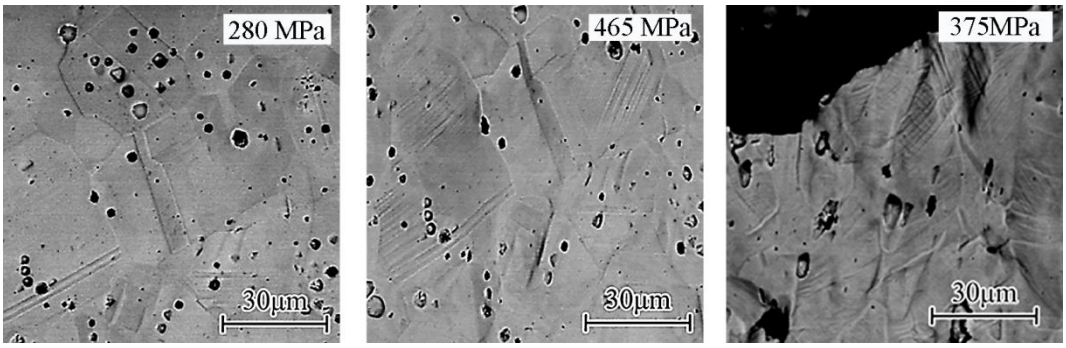

Figure 10 From left to right: evolution of the V-V parts microstructure with strain at approximately the yield point, the ultimate tensile stress and the rupture strength.

The fracture surfaces of all the tensile tested specimens were examined by SEM. Resultant fractography images are shown in Figure 11. In principal, the sintered in vacuum samples exhibited a typical ductile fracture by microvoids coalescence (MVC) based on the presence of dimples initiated at inclusions. These inclusions were sometimes original powder particles that were not sintered due to the presence of an oxide coat that was not reduced with the sintering conditions. This was more evident in the A-V condition (Figure 11b) with dimple sizes around 5µm. Spherical particles were clearly observed in the middle of the rounded dimple with the same size of powder particles. Deformation slip bands were observed in many dimples. Figure 12 shows a magnified image of A-V fracture surface with EDX semi-quantitative elemental analysis at different regions. The element estimation may fall in errors since the surface is rough. However, spherical Invar 36 particles were identified in the middle of the dimple (Figure 12(1)) with a broken oxide shell surrounding the particles (Figure 12(2)). Some silica inclusions were also identified in some dimples (Figure 12(3)).

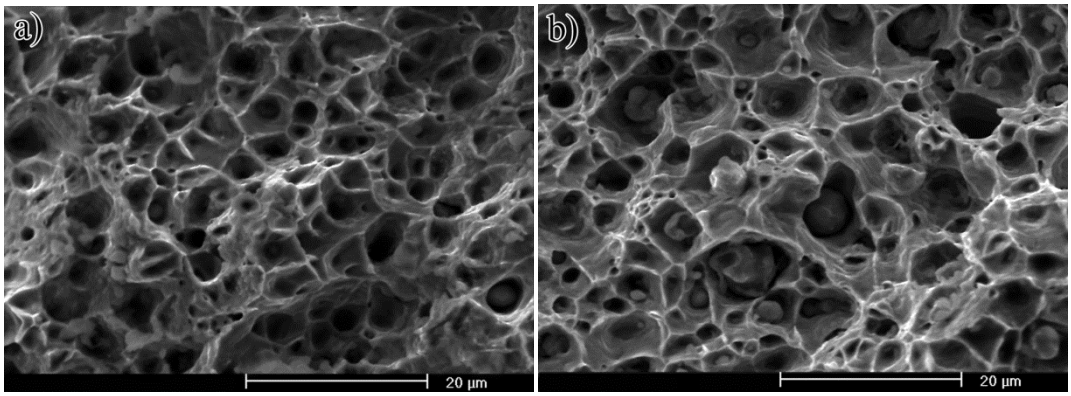

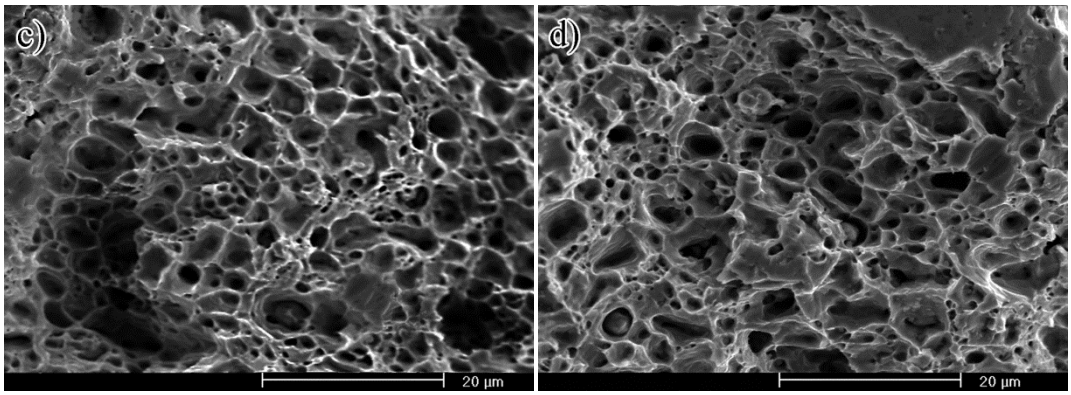

Figure 11 Fracture surfaces of different tensile specimens after micro tensile test: a) V-V, b) A-V, c) V-H and d) A-H.

By contrast the sintered in hydrogen specimen exhibited two modes of fracture: a predominant MVC and a second less ductile mode with some transgranular facets sometimes roughened by slip steps. The dimple sizes in those cases were smaller than sintered in vacuum specimens (around 1µm) most likely they were initiated by sub-micrometer inclusions. Moreover, there were less clear slip bands in the dimples or directly they were not observed. The presence of transgranular facets may be linked with the embrittlement observed in the stress-strain curves of these conditions. Winding regions of apparently dimples clusters were observed in all specimens independently of the sintering atmosphere.

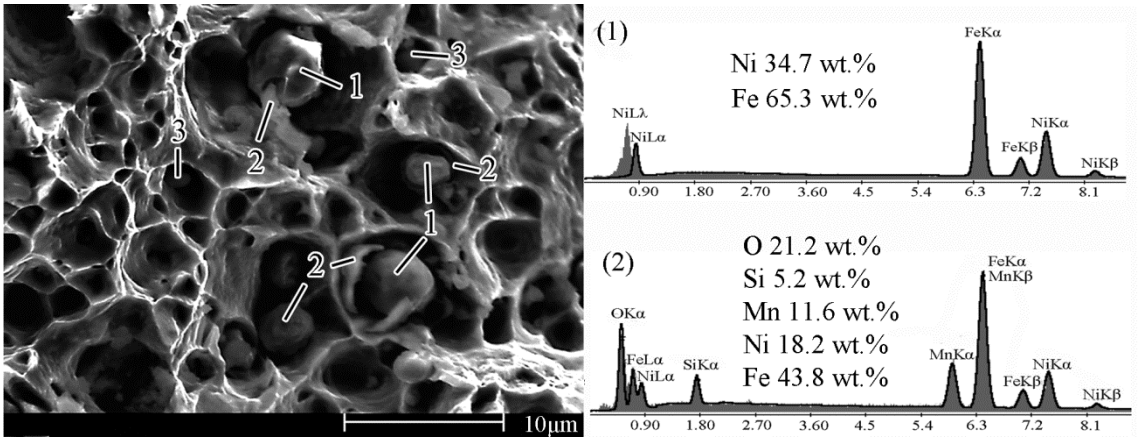

Figure 12 Magnified image of A-V fracture surface accompanied of EDX analysis at different points. (1) Original Invar 36 particle, (2) Possible complex FeNiSiMn oxide shell sourronding original Invar 36 particle, (3) Silica inclusions with a small amount of Mn according to EDX.

4 Conclusions

The effect of debinding and sintering atmospheres of INVAR 36 micro parts was investigated. The following conclusions were drawn:

- Air degraded more effectively CAB during sintering but is responsible of metallic particles oxidation. However these oxides could be reduced employing reductive hydrogen or vacuum atmospheres also aided by carboreductive effect of remaining carbon after debinding.
- The debinding in vacuum atmosphere leaved a high percentage of contaminating carbon source. Residual carbon could be eliminated by pyrolysis with vacuum media or by reductive hydrogen during sintering.
- All combined processing condition leaded to the formation of desirable austenitic microstructure responsible of the low CTE of INVAR 36 and produces similar levels of carbon contamination. This was contrasted by microstructure investigations by SEM, by XRD and element analysis.
- To some extent, resulting mechanical properties meet the standards of an Invar 36 alloy. Presence of none reduced oxides influenced the densification of the micro parts and leaded on a detriment of the mechanical properties.
- The hydrogen atmosphere have demonstrated to be effective for the reduction of oxides and the part densification, but this element has been easily introduced as an interstitial element worsening the ductility, the Curie's temperature and the coefficient of thermal expansion.
- The debinding and sintering in vacuum produced the most equilibrated physical and mechanical properties.

5 Acknowledgements

The authors wish to thank GUZMÁN GLOBAL S.L. and MIMTECH ALFA for their collaboration on the ECOPIM project (ref. IPT-2011-0931-20000) that was funded by the Spanish Ministry of the Economy and Competitiveness. Furthermore, the authors would like to acknowledge the funding provided by CAM-Consejeria de Educación Dir. Gral. Universidades e Investigación in the project ESTRUMAT (ref. S2009/MAT-1585) and the Nacional Project (MAT2012/38650-C02-01).

References

1. V. A. Maslyuk, O. A. Panasyuk, and O. V. Vlasova, *Powder Metallurgy and Metal Ceramics*, 2003, **42**(9-10), 536-539.
2. B. K. Jasthi, W. J. Arbegast, and S. M. Howard, *Journal of Materials Engineering and Performance*, 2009, **18**(7), 925-934.
3. B. Cha, J. M. Jang, W. Lee, S.-H. Ko, S.-H. Son, W. K. You, and J.-S. Lee, *Journal of Ceramic Processing Research*, 2012, **13**, S22-S25.
4. L. Chun-Ting, C. Bi-Shiou, and S. Chi, *IEEE Journal of Selected Topics in Quantum Electronics*, 2006, **12**(5), 970-982.
5. U. M. Attia and J. R. Alcock, *Journal of Micromechanics and Microengineering*, 2011, **21**(4).

6. V. Piotter, W. Bauer, R. Knitter, M. Mueller, T. Mueller, and K. Plewa, *Microsystem Technologies-Micro-and Nanosystems-Information Storage and Processing Systems*, 2011, **17**(2), 251-263.
7. X. Kong, T. Barriere, and J. C. Gelin, *Journal of Materials Processing Technology*, 2012, **212**(11), 2173-2182.
8. C. Quinard, J. Song, T. Barriere, and J. C. Gelin, *Powder Technology*, 2011, **208**(2), 383-389.
9. A. V. Ruban, S. Khmelevskyi, P. Mohn, and B. Johansson, *Physical Review B*, 2007, **76**(1).
10. O. A. Khomenko, *Physics of Metals and Metallography*, 2007, **104**(2), 146-156.
11. V. M. Nadutov, S. G. Kosintsev, E. O. Svystunov, and O. I. Zaporozhets, *Metallofizika I Noveishie Tekhnologii*, 2009, **31**(8), 1021-1034.
12. V. M. Nadutov, S. G. Kosintsev, Y. O. Svystunov, V. A. Tatarenko, and T. V. Yefimova, *Metallofizika I Noveishie Tekhnologii*, 2006, **28**, 39-48.
13. B. S. Kim, K. J. Yoo, B. G. Kim, and H. W. Lee, *Metals and Materials International*, 2002, **8**(3), 247-252.
14. J. Wittenauer: 'Factors affecting the mechanical strength of Fe-36Ni Invar', Invar Effect: A Centennial Symposium, 1996, 231-238.
15. ASM: 'Metals Hadbook:Properties and Selection - Nonferrous Alloys and Pure Metals'; 1979, OH, USA,
16. W. Sokolowski, C. Hsieh, and T. O'Donnell: 'New HP (high purity) Invar 36', 147-156; 1996,
17. A. Vinogradov, S. Hashimoto, and V. I. Kopylov, *Materials Science and Engineering a-Structural Materials Properties Microstructure and Processing*, 2003, **355**(1-2), 277-285.
18. W. Sokolowski, C. Hsieh, and T. O'Donnell: 'New HP (high purity) Invar 36', Invar Effect: A Centennial Symposium, 1996, 147-156.
19. A. A. Gulyaev and E. L. Svistunova, *Scripta Metallurgica Et Materialia*, 1995, **33**(9), 1497-1503.
20. J. Wittenauer, D. L. Yaney, and R. E. Lewis, *Scripta Metallurgica Et Materialia*, 1994, **31**(11), 1531-1536.
21. J. Hidalgo, A. Jimenez-Morales, and J. M. Torralba, *Journal of the European Ceramic Society*, 2012, **32**(16), 4063-4072.
22. S. Minseok, P. Min Soo, K. Jin Kon, C. Il Bum, K. Kyung Ho, S. Hwan Jin, and A. Sangho, *Journal of Materials Science*, 2005, **40**(5), 1105-1109.
23. J. Hidalgo, A. Jimenez-Morales, and J. M. Torralba, *Polymer Degradation and Stability*, 2013, **98**(6), 8.
24. N. Labrador and P. Lefort, *Journal De Chimie Physique Et De Physico-Chimie Biologique*, 1999, **96**(5), 810-829.
25. M. Momeni, C. Gierl, and H. Danninger, *Materials Chemistry and Physics*, 2011, **129**(1-2), 209-216.
26. D. Chasoglou, E. Hryha, and L. Nyborg, *Materials Chemistry and Physics*, 2013, **138**(1), 405-415.
27. W. K. Jozwiak, E. Kaczmarek, T. P. Maniecki, W. Ignaczak, and W. Maniukiewicz, *Applied Catalysis a-General*, 2007, **326**(1), 17-27.
28. M. Imbaby and K. Jiang, *World Congress on Engineering, WCE 2009*, 2009, 536-540.
29. Y. H. Zhao, Y. Z. Guo, Q. Wei, T. D. Topping, A. M. Dangelewicz, Y. T. Zhu, T. G. Langdon, and E. J. Lavernia, *Materials Science and Engineering a-Structural Materials Properties Microstructure and Processing*, 2009, **525**(1-2), 68-77.